High-Performance Quasi-Solid-State Thermogalvanic Cells with Metallized Fibril-Based Textile Electrodes and Structure-Breaking Salts

Jaejin Choi, Jeongmin Mo, Jaemin Jung, Yeongje Jeong, Jinhan Cho,* and Jaeyoung Jang*

Thermogalvanic cells (TGCs) convert heat into electricity through thermoelectrochemical reactions of redox couples, generating a millivolt-scale Seebeck coefficient. However, TGCs based on liquid electrolytes are prone to leakage, whereas quasi-solid-state TGCs (QTCs) using gel-based electrolytes typically have low power outputs due to slow ion diffusion and limited reaction rates. Herein, we present novel strategies for developing high-performance all-flexible QTCs using both metallized fibril-based textile electrodes with extremely large surface area, (specifically Ni textiles), and structure-breaking salts for hydrogel electrolytes. The electrodes are oxidized to create Ni and Ni oxide heterostructures, forming numerous O vacancy defects that enhance redox reactions. Meanwhile, the structure-breaking salts facilitate redox reactions and improve ion diffusion by disrupting water structures in the hydrogel electrolyte. These advancements significantly enhance the performance of the QTCs without the need for precious-metal electrodes, achieving a remarkable maximum power density of 4.05 mW m^{-2} K^{-2} and a record-high effective cell conductivity of 17.3 S m^{-1}, compared to previously reported QTCs. Finally, the proposed QTCs can generate a stable open-circuit voltage and output power for wearable applications owing to the flexibility of the electrodes and electrolyte, achieving successful electronic device operation using body heat from the forearm ($\Delta T \approx 2$ K).

1. Introduction

The rapid development of wearable electronics has sparked significant interest in a new era of energy-harvesting technologies, emphasizing the need for self-powering systems with good flexibility.[1–3] Among various energy-harvesting devices, thermoelectric (TE) generators are promising candidates that produce stable power using ubiquitous temperature gradient (ΔT) without noise and moving parts or relying on weather conditions.[4,5] In particular, thermogalvanic cells (TGCs), which utilize the thermo-electrochemical reactions of redox couples, have received considerable attention owing to their millivolt-scale Seebeck coefficient (S) values (>1 mV K^{-1}). These values are nearly 100 times higher than those of conventional TE materials based on electronic Seebeck effects,[6,7] demonstrating the utility of TGCs for powering electronic devices from low-grade heat waste around room temperature. When a ΔT is applied to a TGC, oxidation and reduction co-occur at the surface of each electrode.[8,9] The reacted products then diffuse to the opposite electrode, undergoing continuous thermo-electrochemical reactions and facilitating sustainable power generation. Additionally, as redox couples, such as ferro-/ferricyanide (FeCN), are composed of naturally abundant elements and inexpensive components, TGCs can be considered a highly cost-effective option within TE technologies.[10] However, using liquid electrolytes in redox couple-based TGCs presents fundamental challenges, such as leakage, that significantly limit their flexible applications, including wearable devices.[3,11]

Flexible and leak-proof quasi-solid-state TGCs (QTCs) have been developed by impregnating the redox couple electrolytes into a polymer matrix, such as hydrogels, to address the issues associated with liquid electrolytes.[12,13] The mechanical properties of the gel electrolytes can be precisely controlled by selecting different types of polymer matrices, ensuring the suitability of the QTCs for wearable applications.[3,12,14] For example, double-network or anisotropic structures within the polymer matrices have been employed to achieve high mechanical strength while maintaining good flexibility.[15–17] Nonetheless, further improvement is still needed for the output performance of QTCs. The normalized areal power density ($P_{max}/(\Delta T)^2$) values of QTCs typically range from 0.002 to 11.9 mW m^{-2} K^{-2},[7,12–30] which are relatively lower than those of liquid-state TGCs, typically ranging from 0.4 to 16.5 mW m^{-2} K^{-2}.[8–11,31–37] Such lower performance is mainly ascribed to the polymer chains that restrict the

J. Choi, J. Jung, Y. Jeong, J. Jang
Department of Energy Engineering
Hanyang University
222, Wangsimni-ro, Seongdong-gu, Seoul 04763, Republic of Korea
E-mail: jyjang15@hanyang.ac.kr
J. Mo, J. Cho
Department of Chemical and Biological Engineering
Korea University
145, Anam-ro, Seongbuk-gu, Seoul 02841, Republic of Korea
E-mail: jinhan71@korea.ac.kr

The ORCID identification number(s) for the author(s) of this article can be found under https://doi.org/10.1002/aenm.202404151

**ADVANCED
SCIENCE NEWS**

www.advancedsciencenews.com

**ADVANCED
ENERGY
MATERIALS**

www.advenergymat.de

movement of redox couples, thereby limiting the electrochemical reactions at the electrodes and the effective cell conductivity.[15,18] Consequently, QTCs often do not provide stable output current over time.[12,20]

One of the proposed methods to improve the output power of QTCs is using electrolyte additives, such as guanidinium chloride or urea,[7,16,28–30] which can increase the S by modulating the entropy of redox couples.[9,10,35,36] However, the electrodes of these QTCs are either based on noble metals, such as platinum and gold, in the form of wires and sheets or inflexible carbon papers, which can diminish the advantages of low-cost and flexible gel electrolytes.[7,16,28–30] This is probably because the organic compound additives can cause undesirable side reactions with common non-precious metal electrodes (Figures S1 and S2, Supporting Information).[38] Therefore, the QTC performance should be improved using non-precious and fully flexible electrode materials.[3,39] Additionally, these electrodes must also be designed considering various factors, such as electrical conductivity, hydrophilicity, and specific active surface area.[12,24,27] Moreover, addressing the issue of slow ion diffusion within polymer gel electrolytes is essential.[15,18]

The gel electrolyte and electrode should be developed complementary to facilitate electrochemical reactions and enhance the device performance. In particular, electrodes should efficiently extract current from diffused redox couples, and gel electrolytes should ensure sufficient diffusion of these redox couples to the electrode.[40] To this end, electrodes should possess an extremely large surface area, hydrophilic surface, bulk metal-like electrical conductivity, and high catalytic activity.[3,39] However, to the best of our knowledge, the reported QTC electrodes have yet to meet all these criteria simultaneously. For instance, flexible 3D carbon cloth electrodes have relatively low catalytic activity and highly hydrophobic surfaces,[14,29] and their sheet resistances (>5 Ω sq^{-1}) are much higher than those of bulk metal-based electrodes (< 0.1 Ω sq^{-1}).[41,42]

Meanwhile, the diffusion of redox couples in a gel electrolyte is strongly influenced by the extent of H bonding interaction. In aqueous media, mobile ions diffuse through H bonds among water molecules,[43] and the addition of specific ions can either promote or disrupt these H bonds. For example, adding "structure-breaking" ClO_4^- anions to a poly(ethylene glycol) hydrogel increases the diffusion coefficient of the target material (Eosin Y) by two orders of magnitude.[44] Therefore, structure-breaking ions can markedly increase the number of redox couples that reach the electrodes, thereby enhancing the effectiveness of electrochemical reactions. However, despite these advantages, if the gel electrolyte does not sufficiently wet the electrode or the diffusion of redox couples to the electrode is inadequate (particularly, in the case of highly porous 3D electrodes with a complex structure), the resulting power generation of QTCs will be significantly restricted.[27] Therefore, collaborative efforts to improve both the electrode and the electrolyte are required to achieve high-performance QTCs without using noble-metal components.

In this study, we introduce a noble-metal-free and all-flexible QTC with high power generation and unprecedented effective cell conductivity. This is achieved through the use of metallized fibril-based textile electrodes with extremely large active surface area and the incorporation of structure-breaking salts into hydrogel electrolyetes, which greatly enhance the diffusion of re-

dox couples and promote their redox reactions (**Scheme 1**). We also highlight that our flexible textile electrode exhibits a high electrochemical response due to the abundance of O vacancies and is completely filled with the gel electrolyte from the outside to the inside. To achieve these goals, we first utilized Ni-electrodeposited carbonized cotton textiles (Ni-CCTs) as flexible 3D electrodes. This cost-effective Ni-CCT configuration exhibits an extremely low sheet resistance (<0.05 Ω sq^{-1}) while maintaining a porous structure crucial for enhanced QTC performance. The alkaline treatment on the electrodeposited Ni layers creates a large number of electrochemically active O vacancy defects, further boosting the thermoelectrochemical activity of the QTCs. Furthermore, the Ni electrodeposition onto pristine CCTs formed nanoprotuberant-structured Ni/Ni oxide layers, further increasing the large active surface area of macroporous pristine CCTs. Despite this large surface area, the skeletal mass density of the Ni-CCT electrode was estimated to be ≈1.03 g cm^{-3}, which was considerably lower than that of Ni foam or Ni felt (≈8.91 g cm^{-3}).[45] Second, we incorporated Cs-based structure-breaking salts into poly(acrylamide) (PAM)-based hydrogel electrolytes. These ionic salts enhanced the diffusion and electrochemical activity of the FeCN redox couples by disrupting the hydration shells and H bonds among water molecules. As a result, our fully flexible QTC achieved a record-high effective cell conductivity of 17.3 S m^{-1} among all reported QTCs.[7,12–30] In addition, a remarkable $P_{max}/(\Delta T)^2$ of 4.05 mW m^{-2} K^{-2} was achieved, which is the highest value reported for noble-metal-free QTCs.[12–14,19,24–27,29] These advancements enabled our QTC to power a light-emitting diode (LED) and hygro-thermometer under an extremely low $\Delta T \approx 2$ °C when applied on the forearm, demonstrating its exceptional performance and flexibility in generating stable power from curved heat sources, such as the human body. As our approach is rooted in the structural, interfacial, and electrochemical designs of electrodes and electrolytes, we believe this approach can provide a basis for developing and designing various high-performance electrochemical devices as well as QTCs.

2. Results and Discussion

2.1. Preparation of Ni-Coated Textile Electrodes for All-Flexible QTCs

Ni-CCT electrodes with large active surface areas for QTCs were prepared by first carbonizing natural cotton textiles composed of numerous cellulose fibrils (Scheme 1). Carbonization temperature greatly affects the chemical and physical structures and electrical properties of CCTs.[46,47] As such, we used Raman spectroscopy and analyzed the changes in the microstructural characteristics of the CCTs with increasing carbonization temperature from 550 to 850 °C. **Figure 1a** shows the spectra of all carbonized samples with three distinct peaks at ≈1335, 1581, and 2884 cm^{-1}, corresponding to the D, G, and 2D bands, respectively.[48,49] The D band represents the disordered A_{1g} vibrational mode of the hexagonal carbon structure. In contrast, the G band originates from the E_{2g} vibrational mode of the six-membered aromatic rings.[50] Also, the distinct 2D band at 2400–3100 cm^{-1}, highly sensitive to the defect or heteroatom doping in carbon-based structures, confirms the amorphous structures of carbon-based materials at low carbonization temperatures.[51] In particular,

ADVANCED
SCIENCE NEWS

www.advancedsciencenews.com

ADVANCED
ENERGY
MATERIALS

www.advenergymat.de
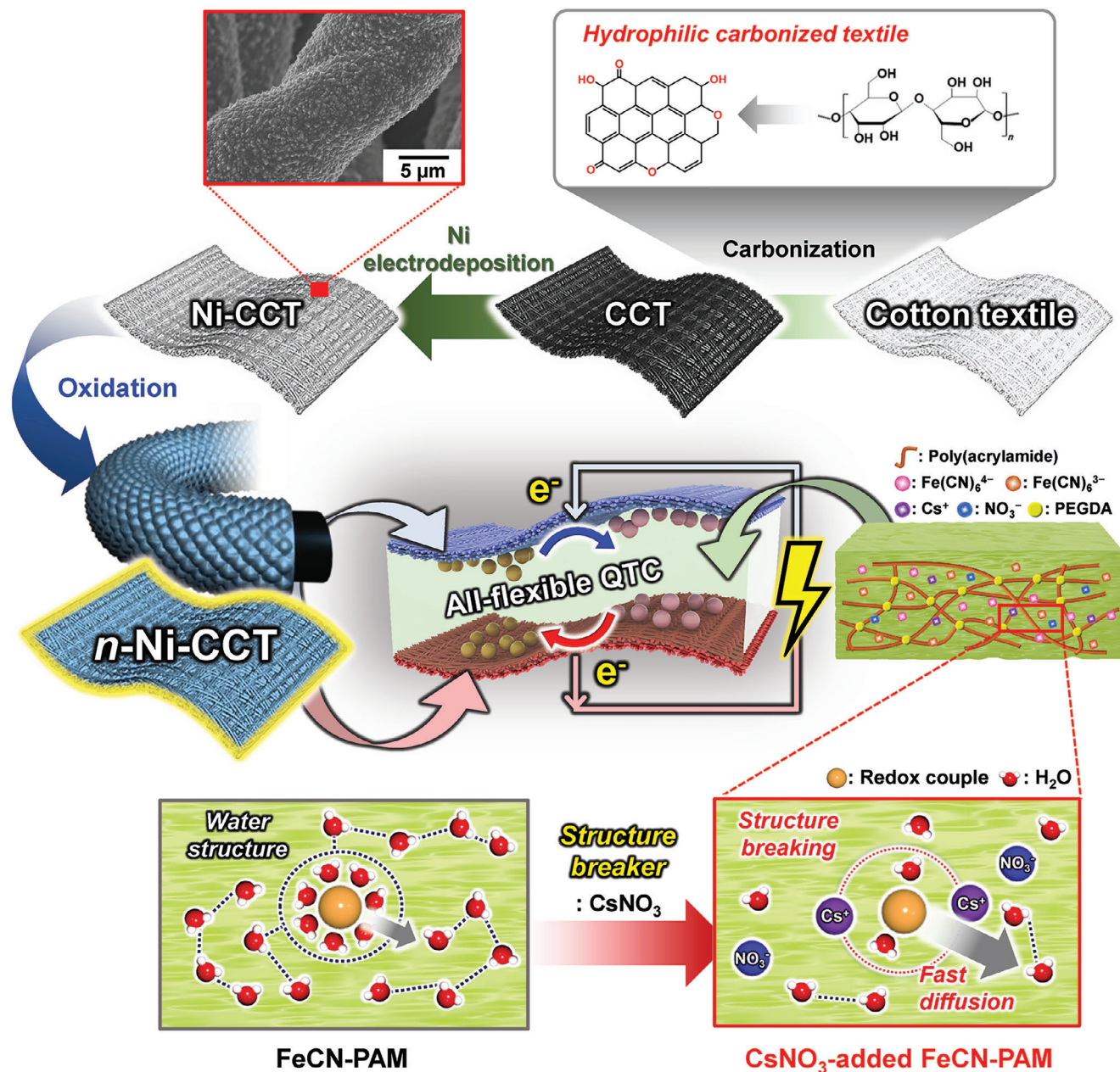
Scheme 1. Design strategy for the fabrication of high-performance, all-flexible QTC. Schematic of the fabrication of *n*-Ni-CCT electrodes, the device structure of the all-flexible QTC, and structure-breaking effect of CsNO₃ salts on the water structures in FeCN-PAM hydrogel electrolyte. The top FE-SEM image and flow chart shows the surface morphology of the Ni-CCT electrode and chemical structure changes of the cotton textile with carbonization, respectively.

the intensity ratio of the D to G bands (I_D/I_G) increases from 0.72 to 1.01. In contrast, the 2D to G bands (I_{2D}/I_G) ratio decreases from 0.51 to 0.22 with increasing carbonization temperature (Figure 1a; Table S1, Supporting Information). These results are consistent with previously reported findings for carbonized softwoods,[52] indicating the enhanced formation of hexagonal ring structures of sp²-hybridized carbon atoms within the carbonized cotton fibers.[53]

X-ray diffraction (XRD) analysis was conducted to investigate further the physical properties of the CCTs (Figure S3, Support-

ing Information). The XRD patterns of the CCTs display two distinct peaks corresponding to the (002) and (100) planes of the carbon structures, regardless of the carbonization temperature. The broad (002) peak at ≈23° indicates partial graphitic ordering within the conjugated carbon structure of the CCTs.[54] In addition, a relatively weak (100) peak is observed at ≈44°, which is associated with the turbostratic structure typically found in disordered carbon materials.[53,55] Notably, as the carbonization temperature is increased from 550 to 950 °C, the electrical conductivity (σ) of the CCTs gradually increased from 2.1×10^{-6} to 1.05

ADVANCED
SCIENCE NEWS

www.advancedsciencenews.com

ADVANCED
ENERGY
MATERIALS

www.advenergymat.de
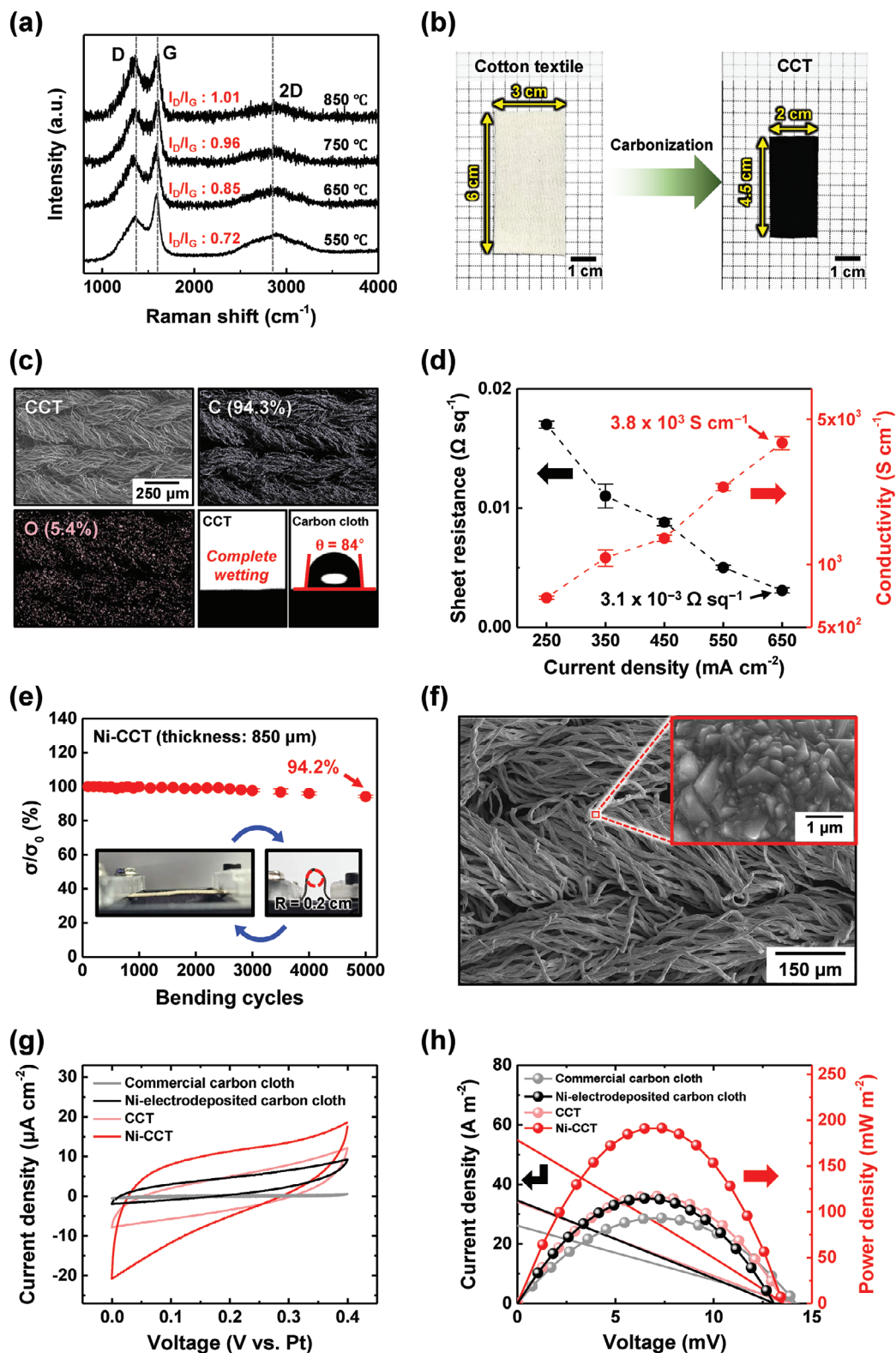
Figure 1. Characterizations of CCTs and Ni-CCTs. a) Raman spectra of CCTs carbonized at different temperatures. b) Photographs of pieces of pristine cotton textile and CCT carbonized at 850 °C. c) FE-SEM and EDS (C and O) images of CCT and water-contact angle (θ) images of CCT and commercial carbon cloth. All images share the same scale bar. d) Sheet resistance and electrical conductivity of the Ni-CCTs as a function of the electrodeposition current density. e) Relative electrical conductivity (σ/σ_0) with bending cycles for the Ni-CCT electrodeposited at 550 mA cm^{-2}. The inset shows Ni-CCT before and after bending with a bending radius (R) of 0.2 cm. f) FE-SEM image of the Ni-CCT. The inset presents a magnified image, showing the surface

**ADVANCED
SCIENCE NEWS**

www.advancedsciencenews.com

**ADVANCED
ENERGY
MATERIALS**

www.advenergymat.de

S cm^{-1} (CCT thickness $\approx$480 µm at 850 °C), and the sheet resistance decreased from 9.8×10^6 to 20 Ω sq^{-1} (Figure S4, Supporting Information). To find an optimal carbonization temperature, we fabricated QTCs using the CCT electrodes and PAM hydrogels with 0.4 M potassium ferro-/ferricyanide (FeCN-PAM) and obtained their current density–voltage (J–V) curves using a custom-built experimental apparatus (Figure S5, Supporting Information). As a result, the QTC with the CCTs carbonized at 850 °C exhibited the highest short-circuit current density (J_{sc}) and maximum power density (P_{max}) (Figure S6, Supporting Information). It should be noted that the J–V curves were measured using a voltage sweep method and therefore the current and power density values are initial values.[9,56,57] The J_{sc} and P_{max} increased with increasing carbonization temperature to 850 °C, and then decreased presumably due to the reduction of the hydrophilicity of the CCT,[58,59] suggesting that 850 °C is the optimal carbonization temperature. After carbonization at 850 °C, the total area and volume of the CCTs decreased by $\approx$50% and 37%, respectively (Figure 1b). This reduction indicates the thermal degradation of the original cellulose functional groups, resulting in conductive CCTs. Despite this thermally induced chemical and structural transformation, the formed CCT maintained its σ value (96.8%) after 5000 bending cycles (Figure S7, Supporting Information). These results strongly suggest the complete transformation of the cotton textile into a highly conductive and flexible substrate with a fibril structure and sufficient σ of the CCTs carbonized at 850 °C for Ni electrodeposition.

We also investigated the hydrophilicity of the CCTs using field-emission scanning electron microscopy (FE-SEM) and energy-dispersive X-ray spectroscopy (EDS). Unlike commercial carbon cloths, which are composed solely of carbon (C) atoms (Figure S8, Supporting Information), the CCTs have a significant amount of oxygen (O) atoms derived from the original cellulose (Figure 1c). These results are consistent with the Raman 2D bands, indicating the presence of heteroatoms (Figure 1a). The presence of O atoms endows the CCT with high hydrophilicity, as confirmed by its complete wetting with a water droplet (pH 5.8), in contrast to the water contact angle of $\approx$84° for commercial carbon cloth (Figure 1c). The hydrophilicity of CCTs greatly facilitates the electrodeposition of metal layers.[60] In the preparation of the Ni-CCTs, a Ni layer was electrodeposited on CCTs for 20 min with varying current densities. Specifically, as the electrodeposition current density was increased from 250 to 650 mA cm^{-2}, the σ of the Ni-CCTs increased from 6.9×10^2 S cm^{-1} to $\approx$$3.8 \times 10^3$ S cm^{-1} (including the total thickness of the Ni-CCTs), while sheet resistance decreased from 1.7×10^{-2} to 3.1×10^{-3} Ω sq^{-1} (Figure 1d). To find an optimal electrodeposition current density, we obtained the J–V curves of the QTCs using the Ni-CCTs and FeCN-PAM electrolytes (Figure S9, Supporting Information). As a result, the QTC with the Ni-CCT electrodeposited at 550 mA cm^{-2} exhibited the highest J_{sc} and P_{max} values, indicating that 550 mA cm^{-2} is the optimal electrodeposition current density. The Ni-CCTs electrodeposited at 650 mA cm^{-2} showed significantly reduced flexibility, likely because of excessive Ni deposition (Figure

S10, Supporting Information). Consequently, the Ni-CCTs electrodeposited at 550 mA cm^{-2} (thickness $\approx$ 850 µm) were selected for further use because of their high σ value and good flexibility, unless otherwise specified.

After 5000 bending cycles at a bending radius of 0.2 cm, the Ni-CCT retained 94.2% of its initial electrical conductivity (σ_0) (Figure 1e), demonstrating high electrical and mechanical stability owing to the strong interfacial interactions between the CCT and Ni layer. Furthermore, the Ni layer was uniformly deposited on the entire CCT surface from the interior to the exterior without notable Ni aggregation, and all Ni-electrodeposited fibrils exhibit a nanoprotuberant surface (Figure 1f; Figure S11, Supporting Information). In contrast, Ni electrodeposition on a hydrophobic commercial carbon cloth (Ni-electrodeposited carbon cloth) resulted in an inhomogeneous Ni coating concentrated on the outermost surface (Figure S12, Supporting Information) and a high water-contact angle of 75° (Figure S13, Supporting Information).

Another notable feature of the Ni-CCTs is their significantly enhanced ion-adsorption capability owing to the nanostructured Ni layer. We conducted cyclic voltammetry (CV) on four different electrodes, namely CCT, Ni-CCT, commercial carbon cloth, and Ni-electrodeposited carbon cloth, using a PAM-based hydrogel with aqueous electrolytes (1 M KNO$_3$) to investigate the effective surface areas for ion adsorption. Among these, the Ni-CCT has the largest CV curve area, ascribed to its hydrophilic surface and nanoprotuberant/macroporous fibril morphology that offers numerous adsorption sites (Figure 1g; Figure S14, Supporting Information).[61,62] The QTC with Ni-CCT electrodes has the highest short-circuit current density and maximum power density (P_{max}) (Figure 1h), corresponding to the CV results (Figure 1g). These findings demonstrate that the hydrophilic carbonization-driven electrodeposition approach is highly effective for producing highly conductive and hydrophilic textile-based QTC electrodes.

2.2. Optimization of Oxidized Ni-CCT Electrodes by Controlling the Defect Ratio

As Ni oxides, such as NiO, Ni(OH)$_2$, and NiOOH, can greatly affect the electrical and electrochemical activity in aqueous electrolyte media, precise control over the oxide composition of electrodeposited Ni is crucial. The electrodeposited Ni layer of the Ni-CCTs was treated with an alkaline solution (1 M KOH) for various soaking times of 0–3 h, designated as n-Ni-CCT (where n is the oxidation time in hours), to achieve the control of the oxide composition of electrodeposited Ni.

The composition and chemical state of the n-Ni-CCT electrodes were analyzed using Raman spectroscopy and X-ray photoelectron spectroscopy (XPS). The Raman spectrum of the Ni-CCT reveals two oxide states of NiO and β-Ni(OH)$_2$ originating from the native oxide layers (**Figure 2a**).[63–65] After oxidation for 0.5 h, distinct NiO peaks at 800–1200 cm^{-1} broadened, and a new O–H bending peak appears at 1635 cm^{-1}, suggesting the formation

morphology. g) CV curves of CCT, Ni-CCT, and pristine and Ni-electrodeposited commercial carbon cloth (scan rate: 50 mV s^{-1}). h) Output current and power densities versus input voltage of all-flexible QTCs at ΔT = 10 K using various electrodes: CCT, Ni-CCT, and pristine and Ni-electrodeposited commercial carbon cloth.

ADVANCED
SCIENCE NEWS

www.advancedsciencenews.com

ADVANCED
ENERGY
MATERIALS

www.advenergymat.de
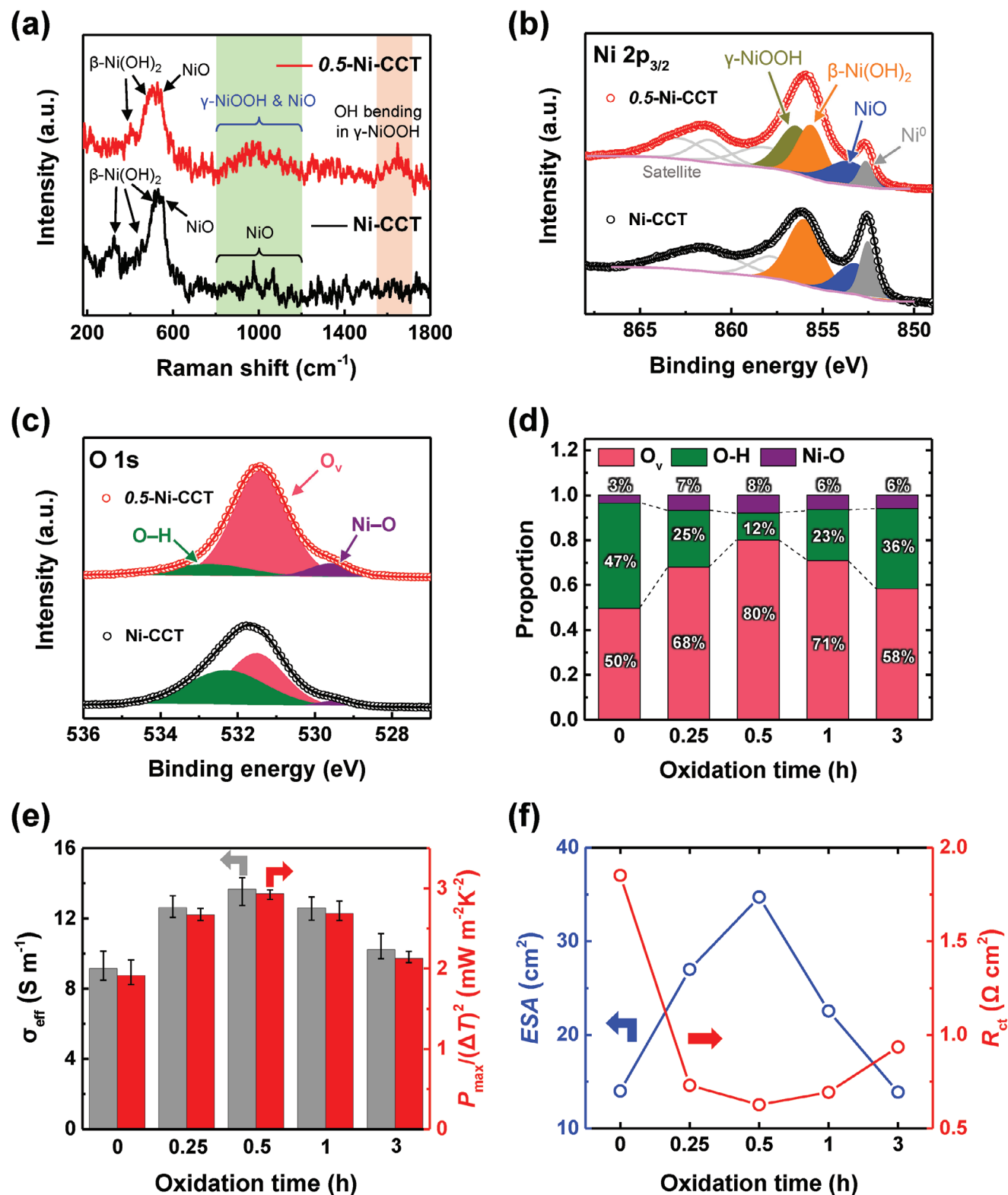
Figure 2. Optimization of oxidation time for *n*-Ni-CCT electrodes. a) Raman and (b) Ni 2p$_{3/2}$ XPS spectra of the Ni-CCT and *0.5*-Ni-CCT. c) O 1s XPS spectra of the Ni-CCT and *0.5*-Ni-CCT. d) Proportions of O$_v$, O–H, and Ni–O with the oxidation time of *n*-Ni-CCTs. e) Plots of σ_{eff} and $P_{max}/(\Delta T)^2$ versus the oxidation time for all-flexible QTCs using *n*-Ni-CCTs. The σ_{eff} and $P_{max}/(\Delta T)^2$ values are average values of the measured values at different ΔT of 5, 10, and 15 K. f) Plots of R_{ct} and *ESA* over the oxidation time for all-flexible QTCs using *n*-Ni-CCTs.

**ADVANCED
SCIENCE NEWS**

www.advancedsciencenews.com

**ADVANCED
ENERGY
MATERIALS**

www.advenergymat.de

of γ-NiOOH.[65,66] Furthermore, we observed the compositional change from the Ni $2p_{3/2}$ XPS spectra of the pristine Ni-CCT and 0.5-Ni-CCT (Figure 2b). The Ni $2p_{3/2}$ XPS spectra of both Ni-CCT samples exhibit three distinct peaks at 852.5 eV (Ni^0), 853.6 eV (NiO), and 856 eV (β-Ni(OH)$_2$). Meanwhile, the spectrum of the 0.5-Ni-CCT has an additional peak corresponding to γ-NiOOH at 856.6 eV.[67,68] Therefore, the Raman and XPS spectra confirmed that the immersion of the Ni-CCTs in a KOH solution led to the formation of γ-NiOOH in n-Ni-CCTs.

We compared the relative changes in the composition ratios of Ni^0, NiO, β-Ni(OH)$_2$, and γ-NiOOH depending on the oxidation time, as derived from the peak areas of the deconvoluted Ni $2p_{3/2}$ XPS spectra (Figure S15, Supporting Information). With increasing oxidation time, the intensity ratio of the β-Ni(OH)$_2$ peak decreases, whereas that of the γ-NiOOH peak gradually increases. After oxidation for 0.5 h, the ratio among the three oxides (i.e., NiO, β-Ni(OH)$_2$, and γ-NiOOH) was the most balanced, suggesting the ample defect sites provided by the heterostructures on the surface of the electrodeposited Ni layer.[69,70] These defect sites modulate the electronic states of the surface Ni layer, improving the catalytic activity.[71,72] The defect sites in n-Ni-CCTs were quantified by analyzing the O 1s XPS spectra (Figure 2c; Figure S16, Supporting Information). The O 1s peaks were deconvoluted into three component peaks corresponding to Ni–O, O vacancy (O$_v$), and O–H.[73–75] The area associated with O$_v$ significantly increases after oxidation for 0.5 h; however, it decreases with further oxidation (Figure 2d).[76,77] Generally, O vacancies in metal oxides can act as n-type dopants, introducing electronic states near the conduction band minimum, endowing semiconductive properties to insulating oxides.[72,78–80] In other words, O vacancy generation results in two electrons per missing O atom, which enhances both the electrochemical activity and electrical conductivity of metal oxides.[72,78–80] These findings suggest that 0.5-Ni-CCTs is the optimal condition, with the maximum number of O$_v$ and the most balanced oxide ratio.

We fabricated all-flexible QTCs composed of n-Ni-CCTs and FeCN-PAM electrolytes and evaluated their output performance. Similar S values are obtained for all n-Ni-CCT-based QTCs with negligible variations across different temperature gradients (Figure S17, Supporting Information), aligning with previously reported values ($\approx$1.4 mV K^{-1}) of typical TGCs using FeCN as a redox couple.[13–15] We then measured the J–V curves of the all-flexible QTCs at ΔT of 5, 10, and 15 K to determine the average values of effective electrical conductivity (σ_{eff}) and $P_{max}/(\Delta T)^2$ (Figure 2e; Figure S18, Supporting Information). σ_{eff} was calculated by multiplying the slope of each J–V curve by the distance between the top and bottom electrodes. This parameter is crucial for comparing the QTC performance as it accounts for key factors, such as the electrical conductivities of the electrodes, the ionic conductivity of the electrolyte, and charge-transfer reactions at the electrodes.[10,11] Among the all-flexible QTCs, that with the 0.5-Ni-CCT electrodes exhibit the highest σ_{eff} value of 13.9 S m^{-1} and $P_{max}/(\Delta T)^2$ value of 2.98 mW m^{-2}K^{-2} at $\Delta T = 10$ K.

The effects of the defects on the electrode surface on the QTC performance were further elucidated by electrochemical impedance spectroscopy (EIS) and CV (Figures S19 and S20, Supporting Information). The charge-transfer resistance (R_{ct}), an essential indicator of the catalytic activity of the electrode, could be derived from the diameter of the semicircle in the Nyquist plot obtained by EIS.[81,82] Additionally, the electroactive surface area (ESA) was derived from the peak current density in the CV curve using the Randles–Sevcik equation (Note S1, Supporting Information).[11,83] As shown in Figure 2d,f, the areal proportion of O$_v$ and electrochemical factors (i.e., ESA and R_{ct}) are highly correlated. In particular, as the O$_v$ proportion increases, ESA increases but R_{ct} decreases, suggesting the increased redox reactions on the electrode surface with a higher density of defect sites.[71,72,76–80] Consequently, the 0.5-Ni-CCT electrodes, which have a larger number of O$_v$ defects, provide more effective reaction sites and exhibit higher catalytic activity with FeCN redox couples. In contrast, the excessively oxidized electrodes with fewer O$_v$ defects have less and weaker reactions with the redox couples and low σ_{eff}.[76,84,85] The FE-SEM images of the n-Ni-CCTs reveal the decreased roughness of the electrode surface with increasing oxidation time, reducing the surface areas (Figure S21, Supporting Information). These results demonstrate that the structural and electrochemical electrode design is crucial for enhancing the σ_{eff} and $P_{max}/(\Delta T)^2$ of all-flexible QTCs.

2.3. Structure-Breaking Salts for Enhancing Diffusion of FeCN Redox Couple

The power output of the all-flexible QTCs was further improved by controlling and optimizing the polymeric electrolyte to enhance the diffusion of redox couples and their redox reactions. Previous studies have demonstrated that structure-breaking ions can facilitate ion diffusion by disrupting the H bonding among water molecules.[43,44] Marcus introduced a structural factor, ΔG_{HB}, which quantifies the ability of added ions to break H-bonded structures among water molecules in aqueous solutions.[86,87] ΔG_{HB} effectively determines the effect of specific ions on the H bonding among water molecules. Specifically, ions with a negative ΔG_{HB} value act as structure breakers for H-bonded networks, whereas those with a positive ΔG_{HB} value act as structure makers, promoting H bonding.

We first investigated the ΔG_{HB} values of various additive anions. **Figure 3a** shows the ΔG_{HB} values of commonly used additive anions, namely NO$_3^-$, SO$_4^{2-}$, and OAc$^-$, for electrochemical devices.[86–88] Among these anions, NO$_3^-$ has the most negative ΔG_{HB} value, indicating strong structure-breaking properties. OAc$^-$ has a positive ΔG_{HB} value, suggesting its structure-making properties, whereas SO$_4^{2-}$ has a relatively moderate negative ΔG_{HB} value. Cs$^+$, a well-known structure-breaking cation that enhances the catalytic activity of FeCN redox couples, was selected for the cationic counterpart.[32,89,90] Cs$^+$ effectively breaks H bonds and disrupts the formation of H-bonded networks among water molecules in the hydration shell of FeCN redox couples compared to other alkali metal cations owing to its large ion size and low charge density.[91] Therefore, three different Cs-based salts, namely CsNO$_3$, Cs$_2$SO$_4$, and CsOAc, were used to investigate their effects on the water structure in hydrogel electrolytes and QTC performance. Incorporating these three salts into the FeCN-PAM electrolytes slightly increased S from 1.40 to 1.44 mV K^{-1}, regardless of the salt types (Figure S22, Supporting Information). This minimal change is ascribed to the similar interactions between the alkali metal cations (Cs$^+$) and two FeCN anions.[10] However, σ_{eff} increases considerably with the
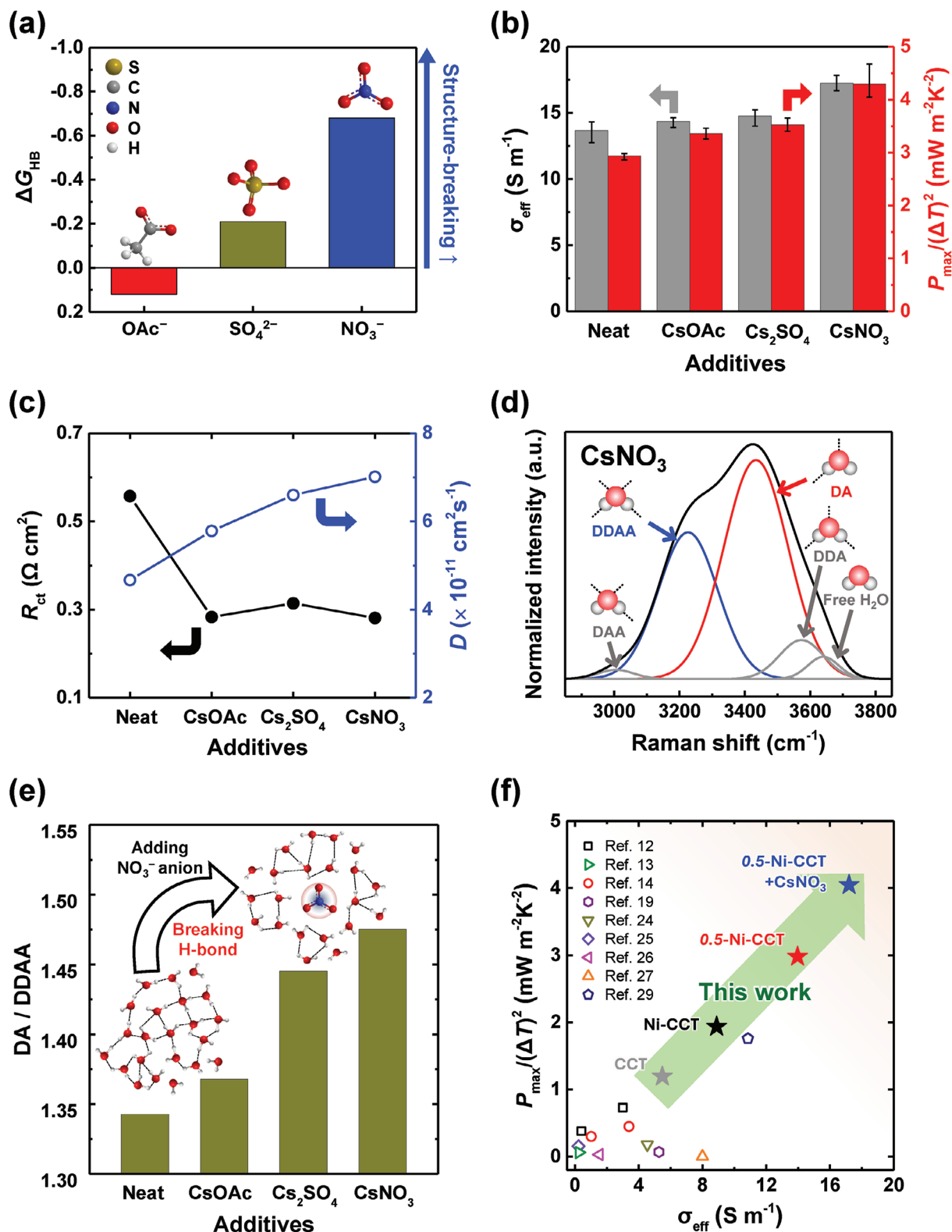
Figure 3. Structure-breaking salts for high-performance all-flexible QTC. a) ΔG_{HB} values for OAc^-, SO_4^{2-}, and NO_3^- anions. b) σ_{eff} and $P_{max}/(\Delta T)^2$ and (c) R_{ct} and D of all-flexible QTCs using the 0.5-Ni-CCT electrodes and FeCN-PAM hydrogel electrolytes with and without additives. The σ_{eff} and $P_{max}/(\Delta T)^2$ values are average values of the measured values at different ΔT of 5, 10, and 15 K. d) Raman O–H stretching spectrum and its deconvoluted spectra for aqueous potassium ferrocyanide solution (0.01 M) with $CsNO_3$ salt (0.8 M). The inset shows the five types of H-bonded water structures (Figure S29, Supporting Information). e) DA/DDAA ratios of the FeCN-PAM hydrogel electrolytes with and without additives. The inset illustrates the breakage

**ADVANCED
SCIENCE NEWS**

www.advancedsciencenews.com

**ADVANCED
ENERGY
MATERIALS**

www.advenergymat.de

addition of these salts (Figure 3b; Figure S23, Supporting Information), which is correlated with the ΔG_{HB} values of the anions (Figure 3a), suggesting that the water structure can affect the output performance of all-flexible QTCs. The optimal salt concentration was set as 0.1 M, according to the QTC measurements with different CsNO$_3$ concentrations (Figure S24, Supporting Information).

The relationship between the water structure and reaction–diffusion kinetics was further explored by EIS measurements on the QTCs using FeCN-PAM electrolytes before and after adding the salts (Figure S25, Supporting Information). We extracted two key electrochemical factors from the Nyquist plots, namely R_{ct} and diffusion coefficient (D). The D values were extracted from the low-frequency region (detailed fitting information is provided in Figure S26, Supporting Information and explained in Note S2, Supporting Information).[92,93] R_{ct} decreased after the salt addition (Figure 3c), which can be ascribed to the structure-breaking properties of the Cs$^+$ cations, which facilitate the charge transfer of redox couples by disrupting the FeCN hydration shell. Meanwhile, the D values of FeCN vary depending on the type of additive salts used. The CsNO$_3$-added FeCN-PAM electrolyte has the highest D value of 7.01×10^{-11} cm^2 s^{-1}, whereas the CsOAc-added FeCN-PAM electrolyte has the lowest D value of 5.78×10^{-11} cm^2 s^{-1}. The effectiveness of CsNO$_3$ salts for FeCN-PAM electrolytes was confirmed with n-Ni-CCT electrodes with various oxidation times (Figure S27, Supporting Information).

The effect of the ionic salts on the water structure in each electrolyte was investigated by comparing the Raman spectra of the aqueous electrolytes containing FeCN with and without additive salts (Figure 3d; Figure S28, Supporting Information). The Raman spectra exhibit water molecules' O–H vibrational peaks corresponding to the H-bonded structures.[94–96] The addition of structure-breaking ions alters these O–H vibrational peaks, reflecting the changes in the H-bonded water structures. After normalizing the spectra of each sample to their maximum value, we deconvoluted the O–H peak area. We identified distinct sub-bands representing the five types of H-bonded water structures (Figure S29, Supporting Information).[94–96] The effect of the salts on the H-bonded water structure was investigated by comparing the intensity ratios of two dominant water structures, namely single donor–single acceptor (DA) and double donor–double acceptor (DDAA). The DA structure, corresponding to a chain-like arrangement of water molecules, has fewer H bonds than the tetrahedral DDAA structure. Therefore, the DA/DDAA ratio can quantitatively indicate the extent of disruption in the hydrogen-bonded structures.[95,96] The CsNO$_3$-added electrolyte has the highest DA/DDAA ratio. In contrast, the CsOAc-added electrolytes have the lowest DA/DDAA ratio (Figure 3e; Figure S30, Supporting Information). As the NO$_3^-$ anions are the most effective in disrupting the H-bonded structure, it is expected to facilitate the diffusion of FeCN redox couples and enhance the σ_{eff} of the QTCs. Additionally, the C≡N stretching bands in the Raman spectra positively shifted with salt addition (Figure S31, Supporting Information). Such positive shifts of similar magnitude indicate that the Cs$^+$ cations effectively disrupt the

hydration shell of the redox couples (Figure S32, Supporting Information).[89] The UV–vis spectra of FeCN solutions with and without CsNO$_3$ salt were also obtained (Figure S33, Supporting Information), revealing that the absorption peaks of FeCN also positively shifted with salt addition due to the disruption of the hydration shell of the redox couples.[9,97]

We demonstrated the effectiveness of the strategies for improving the output power of all-flexible QTCs by optimizing the electrode and electrolyte. These qualitatively and quantitatively enhanced the electrochemical reactions between the redox couple and electrode. Specifically, the all-flexible QTC with the 0.5-Ni-CCT electrodes and CsNO$_3$-added FeCN-PAM electrolyte achieved exceptional performance with an σ_{eff} of 17.3 S m^{-1} and $P_{max}/(\Delta T)^2$ of 4.05 mW m^{-2} K^{-2}, which are over 300% higher than those of the QTC using CCT electrodes and electrolyte without added salts (Figure 3f; Table S2, Supporting Information). Our proposed approach achieved record-high σ_{eff} and $P_{max}/(\Delta T)^2$ values for the QTCs not using noble-metal electrodes.[12–14,19,24–27,29] In particular, the σ_{eff} value of 17.3 S m^{-1} surpasses that of all reported QTCs.[7,12–30] Therefore, our approach offers a highly effective solution for enhancing the output performance of all-flexible QTCs without relying on precious-metal electrodes.[98]

2.4. Body-Heat Energy Harvesting Using All-Flexible QTC

Finally, we demonstrated the feasibility of our QTCs as an energy-harvesting device that harnesses energy from human body heat. Notably, we highlighted the suitability of our all-flexible QTCs for wearable TE devices owing to the high flexibility of the electrodes and hydrogel electrolyte (Figure 1e; Figures S7 and S34, Supporting Information). The addition of redox couples and salts to PAM hydrogels resulted in reduced stretchability, similarly with previous reports.[7,16] However, CsNO$_3$-added FeCN-PAM electrolytes maintained sufficient mechanical properties for use as flexible and leak-free QTCs. Before using QTC for a wearable device, we first evaluated the sustainability of its output performance over a range of ΔT values and hundreds of bending cycles. The all-flexible QTC was fabricated using the CsNO$_3$-added FeCN-PAM electrolyte and 0.5-Ni-CCT electrodes. **Figure 4a** shows the J–V curves of the QTC measured with varying ΔT values of 2.5–10.0 K, while the cold-side temperature was maintained at 15 °C. As expected, the output voltage linearly increased with ΔT, whereas the output power increased quadratically.[99] The open-circuit voltage (V_{oc}) increased from 3.7 to 14.4 mV, depicting a linear relationship with ΔT, whereas P_{max} increases from 24.6 to 405.0 mW m^{-2}, demonstrating a quadratic dependence on ΔT. These consistent trends with minimal deviations across the ΔT range (2.5–10.0 K) indicate the good performance of our all-flexible QTCs in diverse thermal environments. We measured the P_{max} of the all-flexible QTC before and after repeated bending cycles with a bending angle of 90° at $\Delta T \approx 2.2$ K (Figure 4b; S35, Supporting Information). After up to 200 bending cycles, the QTC retained its initial P_{max} value ($P_{max,0}$) with slight fluctuations. Therefore, the optimized all-flexible QTC can endure

---

of hydrogen bonds of water in the presence of NO$_3^-$ anion (enlarged image can be seen in Figure S30, Supporting Information). f) $P_{max}/(\Delta T)^2$ versus σ_{eff} for the proposed all-flexible QTCs compared with other QTCs that did not use noble-metal electrodes (Table S2, Supporting Information).

ADVANCED
SCIENCE NEWS

www.advancedsciencenews.com

ADVANCED
ENERGY
MATERIALS

www.advenergymat.de
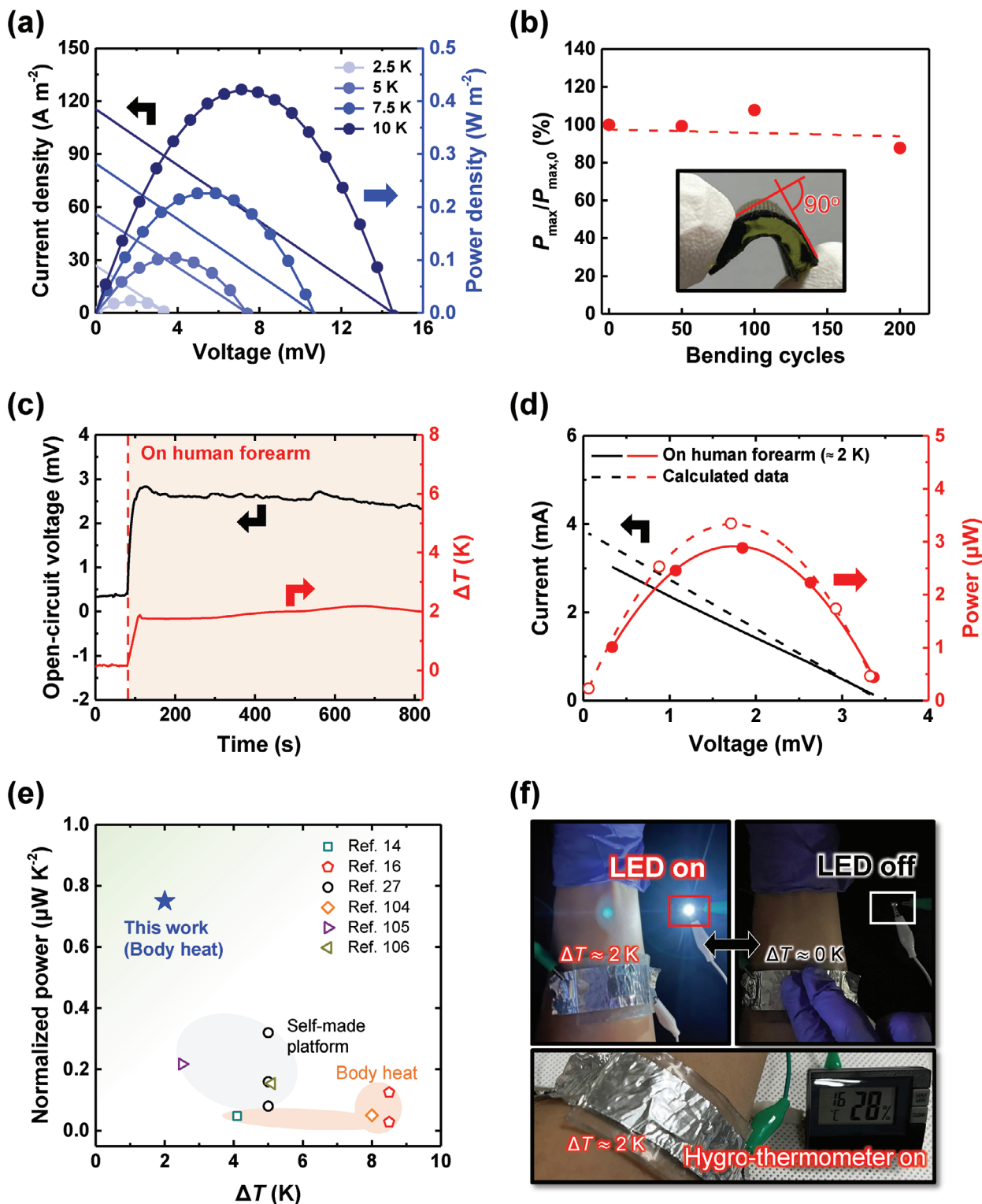
Figure 4. Body-heat harvesting using the high-performance all-flexible QTC. a) Output current and power densities versus input voltage of all-flexible QTCs at ΔT = 2.5, 5.0, 7.5, and 10.0 K. b) Relative maximum power density ($P_{max}/P_{max,0}$) throughout the bending cycles (bending angle ≈ 90°). c) Time-dependent V_{oc} and ΔT profiles of all-flexible QTC attached on the forearm of the subject. d) Output current and power versus input voltage of the QTC on the forearm (ΔT ≈ 2 K) and calculated data based on the result in (a) for ΔT = 2 K. e) Comparison of normalized power of our all-flexible QTC with other reported QTCs and QTC modules operated using body heat or self-made platforms (Table S3, Supporting Information). f) Photographs of powering LED and hygro-thermometer via voltage amplifier using our all-flexible QTC from body heat.

**ADVANCED
SCIENCE NEWS**

www.advancedsciencenews.com

**ADVANCED
ENERGY
MATERIALS**

www.advenergymat.de

variable ΔT conditions and harsh mechanical stresses, making it suitable for wearable applications. When the QTC was connected to an external resistance and measured over time, the output voltage and current decreased until saturation, similarly to previously reported QTCs.[12,20] These measurements could be repeated for several cycles and the output energy densities harvested in each cycle are shown in Figure S36 (Supporting Information).[100]

We evaluated the output performance of the all-flexible QTC by attaching it to the forearm (Figure 4c,d). In general, extremely small ΔT in the range of 0.5–8.0 K is applied across TE material in wearable devices on the human body with variations depending on the environments.[101] Therefore, the TE devices need to form conformal contact with the human body to maximize ΔT and produce high power even at such a small ΔT.[102,103] Our all-flexible QTC with textile electrodes and hydrogel electrolyte is well-suited for this purpose, conforming well to the curved surface of the forearm. We monitored the generated ΔT and V_{oc} values across the all-flexible QTC in real time, observing stable values of ≈2 K and 2.6 mV, respectively (Figure 4c). The short-circuit current and maximum power measured on the forearm were similar to those obtained from a custom-built experimental apparatus at the same ΔT (Figure 4d; Figure S5, Supporting Information). The normalized power derived from human body heat is significantly higher than those of previously reported QTCs (Figure 4e; Table S3, Supporting Information).[14,16,27,104–106] These previously reported QTCs employed partially flexible carbon or noble-metal electrodes, such as graphite papers and platinum sheets, which can restrict QTC applications. Furthermore, the QTC placed on a human forearm was connected to an LED or a hygro-thermometer via a commercial voltage amplifier to demonstrate its practical application,[21,107,108] successfully powering these devices solely using human body heat (Figure 4f; Figure S37, Supporting Information). We also tested the device response to temperature changes by placing and removing a finger from the QTC, causing the LED to turn off and on, respectively (Movie S1, Supporting Information). These results highlight the exceptional potential of the all-flexible QTCs based on textile electrodes and structure-breaking ions for powering electronics from various low-grade heat sources, including the human body.

3. Conclusion

In summary, we demonstrated that our QTCs could exhibit high σ_{eff} and $P_{max}/(\Delta T)^2$ values by using highly flexible Ni-CCT electrodes with a large amount of O_v and extremely large active surface areas and incorporating Cs-based structure-breaking salts into hydrogel electrolytes. To this end, these Ni-CCT electrodes were prepared by carbonizing cotton textiles followed by Ni electrodeposition and oxidation, which effectively increased the number of redox-active sites and O_v defects. CsNO$_3$ salts were added to PAM-based hydrogels containing FeCN redox couples for the QTC electrolyte. The structure-breaking anions (NO_3^-) effectively enhanced the diffusion of the redox couples by disrupting the H bonds among water molecules, demonstrating CsNO$_3$ to have the best diffusion enhancement among the tested Cs-based salts. Consequently, the QTC with the 0.5-Ni-CCT textile electrodes and CsNO$_3$-added FeCN-PAM electrolytes achieved a remarkable $P_{max}/(\Delta T)^2$ of 4.05 mW m^{-2}K^{-2} and unprecedented σ_{eff} of 17.3 S m^{-1}. Furthermore, the all-flexible QTC operated ef-

fectively on the human body under a small ΔT value, demonstrating highly stable power generation on a forearm, sufficient for LED and hygro-thermometer operation. Therefore, this study can provide a basis for overcoming the performance limitations of QTCs and expanding their potential applications in harvesting low-grade thermal energy from curved heat sources, even with low ΔT values. We believe that the proposed approach is effective not only for enhancing the QTC performance but also for developing high-performance electrodes and electrolytes for other electrochemical energy harvesting and storage devices.

4. Experimental Section

Materials: Potassium ferricyanide (K$_3$Fe(CN)$_6$, ≥99.0%) was purchased from Alfa Aesar. Potassium ferrocyanide trihydrate (K$_4$Fe(CN)$_6$·3H$_2$O, 98.5–102.0%), CsNO$_3$ (99.99%), Cs$_2$SO$_4$ (99%), CsOAc (99.9%), KNO$_3$ (≥99.0%), acrylamide (≥99%), poly(ethylene glycol) diacrylate (PEGDA, M$_n$ ≈ 700), ammonium persulfate (APS, ≥98%), N,N,N″,N″-tetramethylethylenediamine (TEMED, ≥99.0%), NiSO$_4$ (98%), NiCl$_2$, (99%), H$_3$BO$_3$ (99.5%), and KOH (99.98%) were purchased from Sigma–Aldrich. Guanidinium chloride (99.0%) was purchased from Merck Millipore. All chemicals were used as received without further purification. The cotton textiles were purchased from KohasiD.

Preparation of CCTs: The cotton textiles were first washed with deionized water and then dried in a convection oven at 100 °C for 1 h to remove any residual moisture. Subsequently, the cleaned cotton textiles were carbonized to prepare CCTs by heating to 850 °C at a rate of 3 °C min^{-1} for 4.5 h in a furnace under N$_2$ gas flow. The CCTs were then naturally cooled to room temperature.

Preparation of n-Ni-CCTs: The as-prepared CCTs were immersed in a Watt bath (240 g L^{-1} NiSO$_4$, 45 g L^{-1} NiCl$_2$, and 30 g L^{-1} H$_3$BO$_3$).[109] Ni layers were electrodeposited onto the CCTs (Ni-CCTs) at a current density of 550 mA cm^{-2} for 20 min using a power supply (Ni loading: 70.3 mg cm^{-1}). In this setup, the CCT served as a cathode, and a high-purity Ni plate was used as an anode. The Ni-CCTs were then washed three times with deionized water and dried in a convection oven at 70 °C for 3 h. Subsequently, the cleaned Ni-CCTs were immersed in a 1 M KOH solution contained within a sealed vial under ambient conditions without stirring for 0.25–3 h, followed by washing with deionized water and drying in a convection oven at 70 °C for 3 h.

Preparation of FeCN-PAM and Cs-Based Salt-Added FeCN-PAM Electrolytes: First, acrylamide (2.5 M) as the monomer, PEGDA (0.3 wt.% relative to the monomer) as the crosslinker, APS (0.5 wt.% relative to the monomer) as the initiator, and TEMED (0.25 wt.% relative to the monomer) as the accelerator were completely dissolved in deionized water (15 mL). The mixed solution was then degassed for 10 min, sonicated for 30 min, and cured under UV light (254 nm, 8 W) for 1 h using a UV crosslinker (XL-1000; Spectro-UV). Next, the prepared PAM hydrogel was dehydrated on a hot plate at 60 °C overnight. The fully dehydrated PAM hydrogel was then soaked in a potassium ferro-/ferricyanide aqueous solution (0.4 M) with or without Cs-based salts (0.1 M CsNO$_3$, 0.1 M CsOAc, and 0.05 M Cs$_2$SO$_4$) for 3 days to fabricate either pristine FeCN-PAM or Cs-based salt-added FeCN-PAM electrolytes, respectively. The concentration of Cs$^+$ ions same for each set of experiments were made, and therefore Cs$_2$SO$_4$ was used in half the amounts to the other salts because Cs$^+$ cations mainly disrupt the hydration shell of the redox couples.[32,89] Each hydrogel electrolyte sample was 10 mm wide, 20 mm long, and 2.2 mm high.

Material Characterizations: Raman spectroscopy of the textile electrodes was performed using a Raman spectrometer (LabRam ARAMIS IR2, HORIBA Jobin Yvon), while the electrolytes were analyzed using a micro-Raman spectrometer (DXR3xi, Thermo Fisher Scientific) equipped with a green laser (532 nm, 10 mW). To obtain high-resolution Raman spectra, the concentration of ferrocyanide was reduced to 0.01 M, whereas the concentrations of Cs-based salts were increased to 0.8 M (for CsNO$_3$ and

CsOAc) and 0.4 м (for Cs_2SO_4).[89] XRD patterns were collected using a high-resolution X-ray diffractometer (SmartLab, Rigaku) with monochromatized Cu Kα radiation (λ = 1.54 Å). The morphology and elemental mapping of the textile electrodes were obtained using a field-emission scanning electron microscope (Verios G4UC, Thermo Fisher Scientific). Water contact angles were measured by the sessile-drop method using a contact angle analyzer (Phoenix-300, Surface Electro Optics) equipped with a video capture camera. Sheet resistances were measured by the four-point probe method using a resistivity meter (Loresta GP MCP-T610, Mitsubishi Chemical Analytech). The thicknesses of the textile electrodes were measured using a caliper (547-401A Digimatic Thickness Gauge, Mitutoyo). Electrical conductivities of the textile electrodes were calculated using the data obtained for sheet resistances and thicknesses. Bending tests for the electrodes were conducted using a custom-built bending machine operated by a motion control unit (MR220A, NOVA Electronics), whereas QTCs were analyzed manually. XPS measurements were carried out using an X-ray photoelectron spectrometer (K-Alpha$^+$, Thermo Fisher Scientific) with a monochromatic Al Kα X-ray source (1486.6 eV, operating voltage/current: 12 keV/6 mA). XPS data was deconvoluted using the Avantage software (Thermo Fisher Scientific). UV–vis spectra were recorded using a spectrophotometer (V670, JASCO). To obtain high-resolution UV–vis spectra, the FeCN and $CsNO_3$ solutions were diluted ≈4000 times compared with the concentrations for QTC measurements.[9,10]

Thermogalvanic and Electrochemical Characterizations: All thermogalvanic and electrochemical characterizations of the QTCs were performed using a potentiostat (Autolab PGSTAT302N, Metrohm). A QTC was mounted on a custom-built apparatus to generate a ΔT along the vertical (through-plane) direction (Figure S5, Supporting Information). A PAM hydrogel electrolyte was sandwiched between two textile electrodes and sealed with VHB tapes (3 м) to prevent water evaporation during the measurements. The temperature of each electrode was controlled using two Peltier devices connected to a power supply (Keithley 2200-30-5). Electrode temperatures were monitored with a Keithley DAQ6510 through thermocouples, while the cold side temperature was maintained at 15 °C. All J–V curves were measured using a voltage sweep method (except that for Figure 4c) and therefore the current and power density values are initial values. The power density in the J–V curves was obtained by multiplying each output voltage and measured output current density. For the wearable measurements on a forearm in Figure 4c, the voltage was measured over time at open circuit condition for 800 s. A voltage amplifier (AD620) was used when powering the LED and hygro-thermometer with the QTC on a human forearm. EIS measurements were performed using textile electrodes with FeCN-PAM or Cs-based salt-added FeCN-PAM electrolytes over a frequency range of 100 kHz to 5 Hz with an amplitude of 10 mV at an open-circuit voltage. CV measurements were performed using either a PAM hydrogel with aqueous electrolytes (1 м KNO_3) at scan rates of 10–50 mV s^{-1} (for Figure 1g) or FeCN-PAM electrolytes with a scan rate of 10 mV s^{-1} (for comparison of ESA in Figure 2f and for checking side reactions in Figure S1, Supporting Information). Platinum sheets served as the counter and reference electrodes, whereas test electrodes including textiles were used as the working electrodes for both EIS and CV measurements.

Supporting Information

Supporting Information is available from the Wiley Online Library or from the author.

Acknowledgements

did not require ethical approval. The human volunteer, who was one of the authors of this article, took part with informed consent, following consideration of any risks involved.

Conflict of Interest

The authors declare no conflict of interest.

Data Availability Statement

The data supporting the findings of this study are available from the corresponding authors upon reasonable request.

[1] C. Zhang, Q. Zhang, D. Zhang, M. Wang, Y. Bo, X. Fan, F. Li, J. Liang, Y. Huang, R. Ma, Y. Chen, *Nano Lett.* **2021**, *21*, 1047.

[2] X. Wang, L. Dong, H. Zhang, R. Yu, C. Pan, Z. L. Wang, *Adv. Sci.* **2015**, *2*, 1500169.

[3] Y. Q. Liu, H. B. Wang, P. C. Sherrell, L. L. Liu, Y. Wang, J. Chen, *Adv. Sci.* **2021**, *8*, 2100669.

[4] S. Kim, Y. J. Na, C. Nam, C. K. Jeong, K. T. Kim, K. I. Park, *Nano Energy* **2022**, *103*, 107824.

[5] D. Zhang, Y. Mao, P. Bai, Q. Li, W. He, H. Cui, F. Ye, C. Li, R. Ma, Y. Chen, *Nano Lett.* **2022**, *22*, 3417.

[6] T. J. Abraham, D. R. MacFarlane, J. M. Pringle, *Energy Environ. Sci.* **2013**, *6*, 2639.

[7] D. Zhang, Y. Mao, F. Ye, Q. Li, P. J. Bai, W. He, R. J. Ma, *Energy. Environ. Sci.* **2022**, *15*, 2974.

[8] T. Kim, J. S. Lee, G. Lee, H. Yoon, J. Yoon, T. J. Kang, Y. H. Kim, *Nano Energy* **2017**, *31*, 160.

[9] J. Duan, G. Feng, B. Yu, J. Li, M. Chen, P. Yang, J. Feng, K. Liu, J. Zhou, *Nat. Commun.* **2018**, *9*, 5146.

[10] B. Yu, J. Duan, H. Cong, W. Xie, R. Liu, X. Zhuang, H. Wang, B. Qi, M. Xu, Z. L. Wang, J. Zhou, *Science* **2020**, *370*, 342.

[11] H. Im, T. Kim, H. Song, J. Choi, J. S. Park, R. Ovalle-Robles, H. D. Yang, K. D. Kihm, R. H. Baughman, H. H. Lee, T. J. Kang, Y. H. Kim, *Nat. Commun.* **2016**, *7*, 10600.

[12] Y. Q. Liu, S. Zhang, Y. T. Zhou, M. A. Buckingham, L. Aldous, P. C. Sherrell, G. G. Wallace, G. Ryder, S. Faisal, D. L. Officer, S. Beirne, J. Chen, *Adv. Energy. Mater.* **2020**, *10*, 2002539.

[13] L. Y. Jin, G. W. Greene, D. R. MacFarlane, J. M. Pringle, *ACS Energy. Lett.* **2016**, *1*, 654.

[14] C. Xu, Y. Sun, J. J. Zhang, W. Xu, H. Tian, *Adv. Energy. Mater.* **2022**, *12*, 2201542.

[15] Z. Lei, W. Gao, W. Zhu, P. Wu, *Adv. Funct. Mater.* **2022**, *32*, 2201021.

[16] L. Liu, D. Zhang, P. Bai, Y. Mao, Q. Li, J. Guo, Y. Fang, R. Ma, *Adv. Mater.* **2023**, *35*, 2300696.

[17] X. Shi, L. Ma, Y. Li, Z. Shi, Q. Wei, G. Ma, W. Zhang, Y. Guo, P. Wu, Z. Hu, *Adv. Funct. Mater.* **2023**, *33*, 2211720.

[18] W. Gao, Z. Lei, W. Chen, Y. Chen, *ACS Nano* **2022**, *16*, 8347.

[19] J. Li, S. Y. Chen, Z. L. Han, X. Y. Qu, M. T. Jin, L. L. Deng, Q. Q. Liang, Y. H. Jia, H. P. Wang, *Adv. Funct. Mater.* **2023**, *33*, 2306509.

**ADVANCED
SCIENCE NEWS**

www.advancedsciencenews.com

**ADVANCED
ENERGY
MATERIALS**

www.advenergymat.de

[20] Y. T. Zhou, S. Zhang, M. A. Buckingham, L. Aldous, S. Beirne, C. Wu, Y. Q. Liu, G. Wallace, J. Chen, *Chem. Eng. J.* **2022**, *449*, 137775.

[21] Z. Lei, W. Gao, P. Wu, *Joule* **2021**, *5*, 2211.

[22] Y. Liu, Q. Zhang, G. O. Odunmbaku, Y. He, Y. Zheng, S. Chen, Y. Zhou, J. Li, M. Li, K. Sun, *J. Mater. Chem. A* **2022**, *10*, 19690.

[23] X. Li, X. Xiao, C. Bai, M. Mayer, X. Cui, K. Lin, Y. Li, H. Zhang, J. Chen, *J. Mater. Chem. C* **2022**, *10*, 13789.

[24] N. Li, Z. Wang, X. Yang, Z. Zhang, W. Zhang, S. Sang, H. Zhang, *Adv. Funct. Mater.* **2024**, *34*, 2314419.

[25] Y. Zong, J. Lou, H. Li, X. Li, Y. Jiang, Q. Ding, Z. Liu, W. Han, *Carbohydr. Polym.* **2022**, *294*, 119789.

[26] Y. Jia, S. Zhang, J. Li, Z. Han, D. Zhang, X. Qu, S. Chen, H. Wang, *J. Power. Sources.* **2024**, *602*, 234400.

[27] H. Meng, W. Gao, Y. Chen, *Small* **2024**, *20*, 2310777.

[28] D. Zhang, Y. Fang, L. Liu, Y. Zhou, P. Bai, Q. Li, J. Guo, R. Ma, *Adv. Energy. Mater.* **2024**, *14*, 2303358.

[29] Z. Wu, B. Wang, J. Li, Y. Jia, S. Chen, H. Wang, L. Chen, L. Shuai, *Nano Lett.* **2023**, *23*, 10297.

[30] J. Wang, Y. Song, F. Yu, Y. Zeng, C. Wu, X. Qin, L. Peng, Y. Li, Y. Zhou, R. Tao, *Nat. Commun.* **2024**, *15*, 6704.

[31] L. Zhang, T. Kim, N. Li, T. J. Kang, J. Chen, J. M. Pringle, M. Zhang, A. H. Kazim, S. Fang, C. Haines, D. Al-Masri, B. A. Cola, J. M. Razal, J. Di, S. Beirne, D. R. MacFarlane, A. Gonzalez-Martin, S. Mathew, Y. H. Kim, G. Wallace, R. H. Baughman, *Adv. Mater.* **2017**, *29*, 1605652.

[32] M. A. Buckingham, S. Hammoud, H. X. Li, C. J. Beale, J. T. Sengel, L. Aldous, *Sustainable. Energy. Fuels.* **2020**, *4*, 3388.

[33] K. Wijeratne, M. Vagin, R. Brooke, X. Crispin, *J. Mater. Chem. A* **2017**, *5*, 19619.

[34] F. Zhao, W. Qian, M. Li, W. Li, L. Chen, F. Zhong, W. Huang, C. Dong, *RSC Adv.* **2017**, *7*, 23890.

[35] X. Zhuang, H. Jin, S. Dai, X. Li, W. Guo, Y. Wang, J. Wu, L. Huang, J. Duan, J. Zhou, *Adv. Energy. Mater.* **2023**, *13*, 2302011.

[36] X. Zhuang, H. Jin, B. Yu, H. Wang, Y. Luo, K. Liu, B. Hu, K. Xie, L. Huang, J. Duan, J. Zhou, *J. Mater. Chem. A* **2022**, *10*, 17544.

[37] H. Chen, H. Zou, F. Zhong, M. Qu, S. Zhao, X. Wei, D. Hong, Y. Song, Z. Liu, *Nano Energy* **2024**, *129*, 109992.

[38] H. Amanapu, K. Sagi, L. Teugels, S. Babu, *ECS J. Solid. State. Sci. Technol.* **2013**, *2*, P445.

[39] Y. F. Liu, M. W. Cui, W. Ling, L. K. Cheng, H. Lei, W. Z. Li, Y. Huang, *Energy. Environ. Sci.* **2022**, *15*, 3670.

[40] P. F. Salazar, S. Kumar, B. A. Cola, *J. Appl. Electrochem.* **2014**, *44*, 325.

[41] Z. Weng, Y. Su, D. W. Wang, F. Li, J. H. Du, H. M. Cheng, *Adv. Energy. Mater.* **2011**, *1*, 917.

[42] A. Sahasrabudhe, H. Dixit, R. Majee, S. Bhattacharyya, *Nat. Commun.* **2014**, *9*, 2018.

[43] S. Mohanakumar, S. Wiegand, *Eur. Phys. J. E* **2022**, *45*, 10.

[44] B. Wu, W. Chasse, K. Zick, M. D. Mantle, A. Heise, D. F. Brougham, V. M. Litvinov, *J. Controlled. Release.* **2020**, *327*, 150.

[45] Y. Son, J. Mo, E. Yong, J. Ahn, G. Kim, W. Lee, C. H. Kwon, H. Ju, S. W. Lee, B.-H. Kim, M. Kim, J. Cho, *Appl. Catal. B-Environ.* **2024**, *343*, 123563.

[46] R. Shokrani Havigh, H. M. Chenari, *Sci. Rep.* **2022**, *12*, 10704.

[47] Y. Huang, M. Song, C. Tian, Y. Wu, Y. Li, N. Yan, Y. Qing, *Sustainable. Energy. Fuels.* **2021**, *5*, 6077.

[48] Z. Sun, Z. Yan, J. Yao, E. Beitler, Y. Zhu, J. M. Tour, *Nature* **2010**, *468*, 549.

[49] H. J. Yoon, N. R. Kim, H. J. Jin, Y. S. Yun, *Adv. Energy. Mater.* **2018**, *8*, 1701261.

[50] Y. Wang, D. C. Alsmeyer, R. L. Mccreery, *Chem. Mater.* **1990**, *2*, 557.

[51] C. Wang, X. Li, E. Gao, M. Jian, K. Xia, Q. Wang, Z. Xu, T. Ren, Y. Zhang, *Adv. Mater.* **2016**, *28*, 6640.

[52] O. Paris, C. Zollfrank, G. A. Zickler, *Carbon* **2005**, *43*, 53.

[53] X. Zhou, P. L. Wang, Y. G. Zhang, X. M. Zhang, Y. F. Jiang, *ACS Sustainable. Chem. Eng.* **2016**, *4*, 5585.

[54] Z. Q. Li, C. J. Lu, Z. P. Xia, Y. Zhou, Z. Luo, *Carbon* **2007**, *45*, 1686.

[55] M. M. Hassan, L. Schiermeister, M. P. Staiger, *RSC Adv.* **2015**, *5*, 55353.

[56] S. Kim, J. H. Kwon, Y. Bae, J. Kim, T. Park, H. C. Moon, *Energy. Environ. Sci.* **2024**, *17*, 8102.

[57] S. Wang, Y. Li, M. Yu, Q. Li, H. Li, Y. Wang, J. Zhang, K. Zhu, W. Liu, *Nat. Commun.* **2024**, *15*, 1172.

[58] Z. Xu, Z. Sun, Y. Zhou, W. Chen, T. Zhang, Y. Huang, D. Zhang, *Colloid. Surf. A-Physicochem. Eng. Asp.* **2019**, *582*, 123934.

[59] J. Prías-Barragán, K. Gross, H. Ariza-Calderón, P. Prieto, *Phys. Status Solidi A-Appl. Mat.* **2016**, *213*, 85.

[60] J. Mo, J. Ko, Y. S. Yun, J. Huh, J. Cho, *Energy. Environ. Sci.* **2022**, *15*, 3815.

[61] L.-N. Jin, F. Shao, C. Jin, J.-N. Zhang, P. Liu, M.-X. Guo, S.-W. Bian, *Electrochim. Acta* **2017**, *249*, 387.

[62] J. Jung, E. H. Suh, Y. Jeong, D.-J. Yun, S. C. Park, J. G. Oh, J. Jang, *Chem. Eng. J.* **2022**, *438*, 135526.

[63] A. K. Ramasami, M. V. Reddy, G. R. Balakrishna, *Mater. Sci. Semicond. Process.* **2015**, *40*, 194.

[64] G. Somasundaram, S. Balasubramanian, T. Vaiyapuri, S. Muthiah, J. R. Sivanesan, N. Nesakumar, S. Shanmugam, B. M. Gunasekaran, *ChemistrySelect* **2023**, *8*, 202204418.

[65] C. Johnston, P. Graves, *Appl. Spectrosc.* **1990**, *44*, 105.

[66] Z. Qiu, C.-W. Tai, G. A. Niklasson, T. Edvinsson, *Energy. Environ. Sci.* **2019**, *12*, 572.

[67] Y.-J. Shih, Y.-H. Huang, C. P. Huang, *Electrochim. Acta* **2018**, *263*, 261.

[68] N. Weidler, J. Schuch, F. Knaus, P. Stenner, S. Hoch, A. Maljusch, R. Schäfer, B. Kaiser, W. Jaegermann, *J. Phys. Chem. C* **2017**, *121*, 6455.

[69] Y. Zhou, H. J. Fan, *ACS Mater. Lett.* **2020**, *3*, 136.

[70] M. Yang, M. Zhao, J. Yuan, J. Luo, J. Zhang, Z. Lu, D. Chen, X. Fu, L. Wang, C. Liu, *Small* **2022**, *18*, 2106554.

[71] X. Yan, L. Zhuang, Z. Zhu, X. Yao, *Nanoscale* **2021**, *13*, 3327.

[72] T. Zhang, M.-Y. Wu, D.-Y. Yan, J. Mao, H. Liu, W.-B. Hu, X.-W. Du, T. Ling, S.-Z. Qiao, *Nano Energy* **2018**, *43*, 103.

[73] J. Yao, H. Wan, C. Chen, J. Ji, N. Wang, Z. Zheng, J. Duan, X. Wang, G. Ma, L. Tao, H. Wang, J. Zhang, H. Wang, *Nano-Micro Lett.* **2021**, *13*, 167.

[74] G. Zhao, G. Hai, P. Zhou, Z. Liu, Y. Zhang, B. Peng, W. Xia, X. Huang, G. Wang, *Adv. Funct. Mater.* **2023**, *33*, 2213170.

[75] X. Wang, L. Zhuang, Y. Jia, H. Liu, X. Yan, L. Zhang, D. Yang, Z. Zhu, X. Yao, *Angew. Chem., Int. Ed.* **2018**, *57*, 16421.

[76] W. Yang, X. Yang, J. Jia, C. Hou, H. Gao, Y. Mao, C. Wang, J. Lin, X. Luo, *Appl. Catal. B-Environ.* **2019**, *244*, 1096.

[77] T. Wang, K. Liu, Z. Gao, Z. Zeng, R. Mao, G. Zhu, J. Ni, X. Xu, R. Jia, S. Han, *Ceram. Int.* **2022**, *48*, 19798.

[78] T. Ling, P. Da, X. Zheng, B. Ge, Z. Hu, M. Wu, X.-W. Du, W.-B. Hu, M. Jaroniec, S.-Z. Qiao, *Sci. Adv.* **2018**, *4*, eaau6261.

[79] H.-S. Kim, J. B. Cook, H. Lin, J. S. Ko, S. H. Tolbert, V. Ozolins, B. Dunn, *Nat. Mater.* **2017**, *16*, 454.

[80] B. Liang, G. Zu, Y. Li, X. Wang, C. Song, Z. Huang, X. Huang, L. Yang, S. Li, *J. Alloy. Compd.* **2024**, *993*, 174568.

[81] A. C. Lazanas, M. I. Prodromidis, *ACS Meas. Sci. Au.* **2023**, *3*, 162.

[82] S. Wang, J. Zhang, O. Gharbi, V. Vivier, M. Gao, M. E. Orazem, *Nat. Rev. Method. Prim.* **2021**, *1*, 41.

[83] P. Papakonstantinou, R. Kern, L. Robinson, H. Murphy, J. Irvine, E. McAdams, J. McLaughlin, T. McNally, *Fuller. Nanotub. Carbon. Nanostruct.* **2005**, *13*, 91.

[84] W. Wang, Y. Wang, X. Zhao, Y. Li, H. He, L. Lian, K. Zeng, L. Wu, L. Deng, Y.-N. Liu, *Chem. Eng. Sci.* **2024**, *285*, 119645.

[85] S. Chen, H. Wang, Z. Kang, S. Jin, X. Zhang, X. Zheng, Z. Qi, J. Zhu, B. Pan, Y. Xie, *Nat. Commun.* **2019**, *10*, 788.

[86] Y. Marcus, *J. Solut. Chem.* **1994**, *23*, 831.

[87] Y. Marcus, *Chem. Rev.* **2009**, *109*, 1346.

ADVANCED
SCIENCE NEWS

www.advancedsciencenews.com

ADVANCED
ENERGY MATERIALS

www.advenergymat.de

[88] D. Sheng, X. Liu, Z. Yang, M. Zhang, Y. Li, P. Ren, X. Yan, Z. X. Shen, D. Chao, *Adv. Funct. Mater.* **2024**, *34*, 2402014.

[89] B. Huang, S. Muy, S. Feng, Y. Katayama, Y. C. Lu, G. Chen, Y. Shao-Horn, *Phys. Chem. Chem. Phys.* **2018**, *20*, 15680.

[90] C. F. Schwenk, T. S. Hofer, B. M. Rode, *J. Phys. Chem. A* **2004**, *108*, 1509.

[91] U. Kaatze, *J. Solut. Chem.* **1997**, *26*, 1049.

[92] S. Xu, L. Lu, Q. Zhang, H. Zheng, L. Liu, S. Yin, S. Wang, G. Li, C. Feng, *J. Nanopart. Res.* **2015**, *17*, 381.

[93] Y. Sun, J. Tang, K. Zhang, X. Yu, J. Yuan, D.-M. Zhu, K. Ozawa, L.-C. Qin, *RSC Adv.* **2021**, *11*, 34152.

[94] Q. Sun, *Vib. Spectrosc.* **2009**, *51*, 213.

[95] C. Choe, J. Lademann, M. E. Darvin, *Analyst* **2016**, *141*, 6329.

[96] Y. Kan, Q. Yang, X. Zhang, Y. Zhang, *Coatings* **2020**, *10*, 872.

[97] M. Qiu, S. Long, B. Li, L. Yan, W. Xie, Y. Niu, X. Wang, Q. Guo, A. Xia, *J. Phys. Chem. C* **2013**, *117*, 21870.

[98] S. Jia, W. Qian, P. Yu, K. Li, M. Li, J. Lan, Y.-H. Lin, X. Yang, *Mater. Today. Phys.* **2024**, *42*, 101375.

[99] T. J. Kang, S. Fang, M. E. Kozlov, C. S. Haines, N. Li, Y. H. Kim, Y. Chen, R. H. Baughman, *Adv. Funct. Mater.* **2012**, *22*, 477.

[100] Y. Li, Q. Li, X. Zhang, B. Deng, C. Han, W. Liu, *Adv. Energy. Mater.* **2022**, *12*, 2103666.

[101] F. Suarez, A. Nozariasbmarz, D. Vashaee, M. C. Öztürk, *Energy. Environ. Sci.* **2016**, *9*, 2099.

[102] Y. Wang, L. Yang, X. L. Shi, X. Shi, L. Chen, M. S. Dargusch, J. Zou, Z. G. Chen, *Adv. Mater.* **2019**, *31*, 1807916.

[103] T. S. Lee, S. Nam, J. G. Oh, E. H. Suh, J. Jung, H. Oh, Y. J. Jeong, J. Jang, *Chem. Eng. J.* **2023**, *455*, 140925.

[104] C. Bai, Z. Wang, S. Yang, X. Cui, X. Li, Y. Yin, M. Zhang, T. Wang, S. Sang, W. Zhang, H. Zhang, *ACS Appl. Mater. Interfaces.* **2021**, *13*, 37316.

[105] S.-H. Hong, C.-C. Hsu, T.-H. Liu, T.-C. Lee, S.-H. Tung, H.-L. Chen, J. Yu, C.-L. Liu, *Mater. Today. Energy.* **2024**, *42*, 101546.

[106] C. C. Hsu, Y. T. Lin, S. H. Hong, U. S. Jeng, H. L. Chen, J. Yu, C. L. Liu, *Adv. Sustainable. Syst.* **2024**, *8*, 2400039.

[107] J. Li, S. Chen, Z. Wu, Z. Han, X. Qu, M. Jin, Y. Jia, Z. Zhou, H. Wang, *Nano Energy* **2023**, *112*, 108482.

[108] P. Peng, J. Zhou, L. Liang, X. Huang, H. Lv, Z. Liu, G. Chen, *Nano-Micro Lett.* **2022**, *14*, 81.

[109] O. P. Watts, *Trans. Am. Electrochem. Soc* **1916**, *29*, 395.